

Postprocessing algorithms to minimize fixed-pattern artifact and reduce trigger jitter in swept source optical coherence tomography

Gangjun Liu,^{1,*} Ou Tan,¹ Simon S. Gao,¹ Alex D. Pechauer,¹ ByungKun Lee,² Chen D. Lu,² James G. Fujimoto,² David Huang¹

¹Casey Eye Institute, Oregon Health & Science University, Portland, Oregon, USA

²Department of Electrical Engineering and Computer Science and Research Laboratory of Electronics, Massachusetts Institute of Technology, Cambridge, Massachusetts, USA

*liga@ohsu.edu

Abstract: We propose methods to align interferograms affected by trigger jitter to a reference interferogram based on the information (amplitude/phase) at a fixed-pattern noise location to reduce residual fixed-pattern noise and improve the phase stability of swept source optical coherence tomography (SS-OCT) systems. One proposed method achieved this by introducing a wavenumber shift (k-shift) in the interferograms of interest and searching for the k-shift that minimized the fixed-pattern noise amplitude. The other method calculated the relative k-shift using the phase information at the residual fixed-pattern noise location. Repeating this wavenumber alignment procedure for all A-lines of interest produced fixed-pattern noise free and phase stable OCT images. A system incorporating these correction routines was used for human retina OCT and Doppler OCT imaging. The results from the two methods were compared, and it was found that the intensity-based method provided better results.

©2015 Optical Society of America

OCIS codes: (170.4500) Optical coherence tomography; (170.3880) Medical and biological imaging; (350.5030) Phase.

References and links

1. H. C. Hendargo, R. P. McNabb, A.-H. Dhalla, N. Shepherd, and J. A. Izatt, "Doppler velocity detection limitations in spectrometer-based versus swept-source optical coherence tomography," *Biomed. Opt. Express* **2**(8), 2175–2188 (2011).
2. T. Klein, W. Wieser, L. Reznicek, A. Neubauer, A. Kampik, and R. Huber, "Multi-MHz retinal OCT," *Biomed. Opt. Express* **4**(10), 1890–1908 (2013).
3. B. Vakoc, S. Yun, J. de Boer, G. Tearney, and B. Bouma, "Phase-resolved optical frequency domain imaging," *Opt. Express* **13**(14), 5483–5493 (2005).
4. Y.-J. Hong, S. Makita, F. Jaillon, M. J. Ju, E. J. Min, B. H. Lee, M. Itoh, M. Miura, and Y. Yasuno, "High-penetration swept source Doppler optical coherence angiography by fully numerical phase stabilization," *Opt. Express* **20**(3), 2740–2760 (2012).
5. G. Liu, M. Rubinstein, A. Saidi, W. Qi, A. Foulad, B. Wong, and Z. Chen, "Imaging vibrating vocal folds with a high speed 1050 nm swept source OCT and ODT," *Opt. Express* **19**(12), 11880–11889 (2011).
6. D. C. Adler, R. Huber, and J. G. Fujimoto, "Phase-sensitive optical coherence tomography at up to 370,000 lines per second using buffered Fourier domain mode-locked lasers," *Opt. Lett.* **32**(6), 626–628 (2007).
7. B. Baumann, B. Potsaid, M. F. Kraus, J. J. Liu, D. Huang, J. Hornegger, A. E. Cable, J. S. Duker, and J. G. Fujimoto, "Total retinal blood flow measurement with ultrahigh speed swept source/Fourier domain OCT," *Biomed. Opt. Express* **2**(6), 1539–1552 (2011).
8. B. Braaf, K. A. Vermeer, V. A. D. P. Sicam, E. van Zeeburg, J. C. van Meurs, and J. F. de Boer, "Phase-stabilized optical frequency domain imaging at 1- μ m for the measurement of blood flow in the human choroid," *Opt. Express* **19**(21), 20886–20903 (2011).
9. W. Choi, B. Potsaid, V. Jayaraman, B. Baumann, I. Grulkowski, J. J. Liu, C. D. Lu, A. E. Cable, D. Huang, J. S. Duker, and J. G. Fujimoto, "Phase-sensitive swept-source optical coherence tomography imaging of the human retina with a vertical cavity surface-emitting laser light source," *Opt. Lett.* **38**(3), 338–340 (2013).

1. Introduction

Swept-source OCT (SS-OCT) is able to achieve very high scan speeds and is less susceptible to interferogram fringe washout than spectral domain OCT (SD-OCT) [1, 2]. Therefore, it has advantages for both structural and Doppler OCT imaging. However, in some SS-OCT systems, there is uncertainty in trigger timing so that the starting point of the spectral interferogram acquisition changes from cycle to cycle in wavenumber (k) space. For phase-sensitive OCT measurements such as Doppler OCT, this jitter will reduce the precision of phase measurements. In addition, trigger jitter reduces the effectiveness of subtractive removal of fixed-pattern noise artifacts (lines at fixed depths in OCT B-scans) arising from unintended internal reflections from fiber tips and sample/reference arm optics [3].

A few numerical methods have been proposed to improve the phase stability of SS-OCT systems [3–7]. However, to the best of our knowledge, removal of the residual fixed-pattern noise with these methods has not been demonstrated. Braaf et al. demonstrated an effective method to eliminate the residual fixed-pattern noise and improve the phase stability by resampling the wavenumber using a simultaneously recorded calibration signal from an interferometer [8]. Although effective, this method requires another reference calibration signal as well as another digitizer channel. Thus, the system complexity and cost will be greatly increased. Alternatively, Choi et al. used a narrow band fiber Bragg grating (FBG) to produce a reference dip in acquired interferograms and then shifted the interferograms accordingly [9]. This method requires less modification of an existing system; however, the introduction of a FBG may induce additional power loss and increase system cost.

In this manuscript, we propose solutions to the trigger jitter problem that do not require additional hardware. Internal reflections in the SS-OCT system that cause residual fixed-pattern noise were used in post-processing as a reference to align the interferograms in k -space. These methods eliminated the residual fixed-pattern noise and improved the phase stability of our SS-OCT system. These methods are purely numerical corrections for systems with fixed-pattern noise.

2. Theory and methods

Here, instead of using an averaged background interferogram as the reference interferogram, we use a single background interferogram as the reference interferogram $A_r(n)$, where n is the index of the sampling point for the interferogram and n is linear with wavenumber. Assuming the interferogram of interest $A_s(n)$ is wavenumber shifted relative to $A_r(n)$ and the inverse Fourier transform of $A_r(n)$ is $I_r(z)$, we have

$$A_s(n) = A_r(n - m_s), \quad (1)$$

$$F^{-1}[A_r(n)] = I_r(z), \quad (2)$$

$$F^{-1}[A_s(n)] = I_s(z) = e^{-i\frac{2\pi}{N}m_s z} I_r(z), \quad (3)$$

$$I_{sr}(z) = I_s(z) - I_r(z) = I_r(z) \S(m_s, z), \quad (4)$$

where m_s is the relative wavenumber shift (k -shift) in the sampling points between A_s and A_r , $F^{-1}[\]$ means inverse Fourier transform, $\S(m_s, z)$ is a scaling factor, $\S(m_s, z) = (e^{-i\frac{2\pi}{N}m_s z} - 1)$, and N is the number of wavenumber samples in the interferogram.

If $m_s = 0$, namely that there is no relative k-shift between the two interferograms, the scaling factor $\S(m_s, z) = 0$ and $I_r(z) = 0$. For the cases where $m_s \neq 0$, the amplitude scaling factor $|\S(m_s, z)|$ shows the ratio between $|I_{sr}(z)|$ and $|I_r(z)|$. The amplitude scaling factor is a function of both m_s and z . Figure 1(a) shows the relationship between the amplitude scaling factor $|\S(m_s, z)|$, z , and m_s . For certain m_s , $|\S(m_s, z)|$ is depth dependent. At certain depth, $|\S(m_s, z)|$ is m_s dependent. Figure 1(b) shows the values for real and imaginary parts of the scaling factor $\S(m_s, z)$ at a depth of $z = 0.05N$.

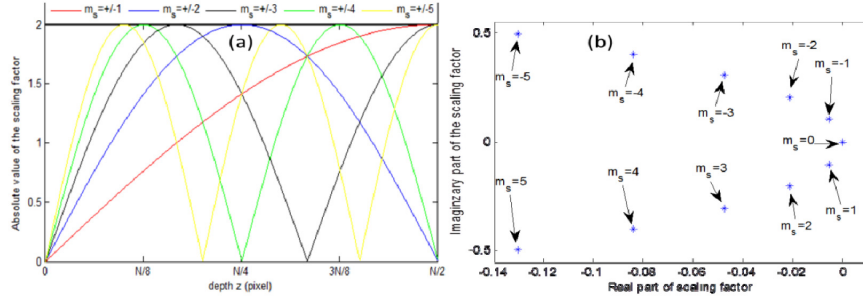


Fig. 1. (a) The relationship between the absolute value of the scaling factor $|\S(m_s, z)|$, depth z , and shift m_s . Here, m_s is the relative k-shift between interferogram of interest A_s and reference interferogram A_r and $m_s \neq 0$. N is the number of wavenumber samples in the interferogram. For a certain m_s , $|\S(m_s, z)|$ is depth dependent. At a certain depth, $|\S(m_s, z)|$ is m_s dependent. (b) The values for real and imaginary parts of the scaling factor $\S(m_s, z)$ at a depth of $z = 0.05N$. At this depth, the value of m_s can be obtained from the value of scaling factor.

For the case of residual fixed-pattern noise at depth z_f , the value of m_s can be deduced from the phases, amplitudes or complex values of $I_r(z_f)$, $I_s(z_f)$ and $I_{sr}(z_f)$. This could be seen from Fig. 1(b). Different k-shift (m_s) will result different scaling factor and the value of m_s can be obtained from value (such as phase, imaginary part or complex value) of scaling factor. Here, we will focus on two methods to obtain m_s . In the first method (method A), m_s can be calculated from the complex values for I_s and I_r at the fixed-pattern noise location and from Eq. (3),

$$m_s = \text{angle}[I_s(z_f)/I_r(z_f)] * N / (2\pi z_f), \quad (5)$$

where $\text{angle}[\]$ is the phase extraction function and phase unwrapping may be necessary for some cases. In the second method (method B), a relative k-shift is introduced in $A_s(n)$, and we search for the k-shift that minimizes $|\S|$ or $|I_{sr}(z_f)|$. Based on Eq. (4), the scaling factor $|\S|$ and $|I_{sr}(z_f)|$ will be zero if there is no relative shift. The shift that minimizes $|\S|$ or $|I_{sr}(z_f)|$ will be the value for m_s . Method A uses only the phase information of the scaling factor and the calculation of m_s is straightforward according to Eq. (5). Method B uses only

the amplitude/intensity information of the scaling factor as a cost function and requires a search scheme.

3. System and results

Here, a SS-OCT retinal imaging system was used for demonstration (Fig. 2). The system uses a swept source laser (Axsun 1050, AXSUN Technologies Inc., Billerica, MA) with a central wavelength of 1050 nm and an A-line rate of 100 kHz. The signal from the balanced detector was sampled with a high speed 400MHz digitizer (Innovative integration X5-400M) using the built-in trigger and clock signals from the Axsun laser. The system has an axial resolution of approximately 7 μm in air and lateral resolution of 23 μm . For each interferogram, there were 1400 useful sample points. Due to unintended reflections from fiber tips, sample/reference arm optics, and an unstable A-line trigger, there were a few fixed-pattern noise locations in the OCT B-scan images. One prominent fixed-pattern noise is around the zero depth position.

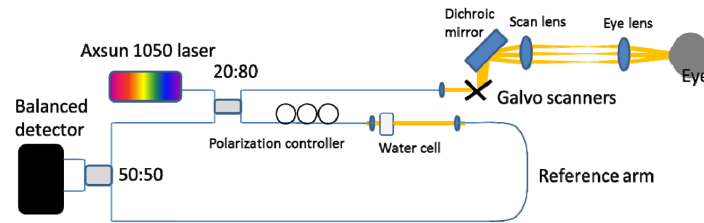


Fig. 2. Schematic of the posterior segment imaging swept-source OCT system.

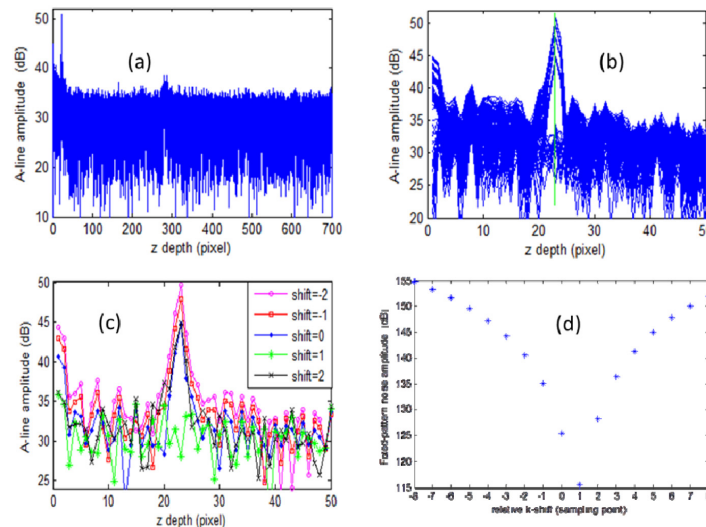


Fig. 3. An arbitrary interferogram from 200 background interferograms was taken as the reference interferogram $A_r(n)$. The reference $A_r(n)$ was then subtracted from the remaining interferograms, and the differences were inverse Fourier transformed. The 200 A-lines were plotted and shown in (a), and the first 50 pixels in depth are shown in (b). The vertical green line in (b) shows the location of the residual fixed-pattern noise. Relative wavenumber (k) shifts were introduced between the reference interferogram and another of the 200 interferograms under evaluation. In (c), the A-line under evaluation were reevaluated after subtracting the shifted interferograms by the reference interferogram. The green line with relative k -shift of 1 shows minimum value at the location of residual fixed-pattern noise (c). The residual fixed-pattern noise amplitude was obtained by summing the A-line amplitude over 3 depth pixels centered at its peak (d). This was then evaluated as a function of the k -shift. The relative trigger jitter in k -space was found as the k -shift at which the fixed-pattern noise amplitude was minimized, +1 in this case.

To illustrate the search scheme of Method B, two hundred consecutive background interferograms were acquired by blocking the sample arm light. An arbitrary interferogram from the 200 interferograms was taken as the reference interferogram $A_r(n)$. This $A_r(n)$ was then subtracted from the remaining interferograms, and the differences were inverse Fourier transformed. The 200 A-lines after the inverse Fourier transform were plotted and shown in Fig. 3(a), and the first 50 pixels in depth are shown in Fig. 3(b). The vertical green line in Fig. 3(b) shows the location of the residual fixed-pattern noise. The depth location for the fixed-pattern noise corresponded to 0.0164N. It can be seen that the amplitudes at the residual fixed-pattern noise location were divided into 5 groups, with the lowest signal group around the noise floor. According to Fig. 1 and Eq. (4), the substantial amplitude difference at the residual fixed-pattern noise location was caused by the trigger jitter. The differences between the groups corresponded to different m_s between the interferograms and reference interferogram $A_r(n)$.

In order to find the value of the relative shift between an interferogram of interest and $A_r(n)$, a relative k-shift was introduced between the reference interferogram and the interferogram under evaluation. The A-line amplitudes at the residual fixed-pattern noise location were evaluated as shown in Fig. 3(c). The residual fixed-pattern noise amplitude was obtained by summing the A-line amplitude over 3 pixels centered at its peak. This was then evaluated as a function of the k-shift. The relative trigger jitter in k-space was found as the k-shift at which the residual fixed-pattern noise was minimized as shown in Fig. 3(d). By repeating this procedure for the rest of the interferograms, we were able to align all the collected interferograms to the reference interferogram.

In order to compare the results of method A and method B, acquired interferograms from a human retina were aligned with both method A and method B. After the alignment of all interferograms, the values for the first or last few wavenumber sample points in some interferograms may be missing. The missing values could be obtained by interpolation, simply adding zeros or using the adjacent data values. However, we found the best image quality was obtained when the first and last few wavenumber sample points were removed before performing further data processing. Then, typical Fourier domain OCT (FD-OCT) data processing procedures were applied. These include background (average of 200 aligned background interferograms) subtraction, Gaussian window spectral shaping, numerical dispersion compensation, and inverse Fourier transform.

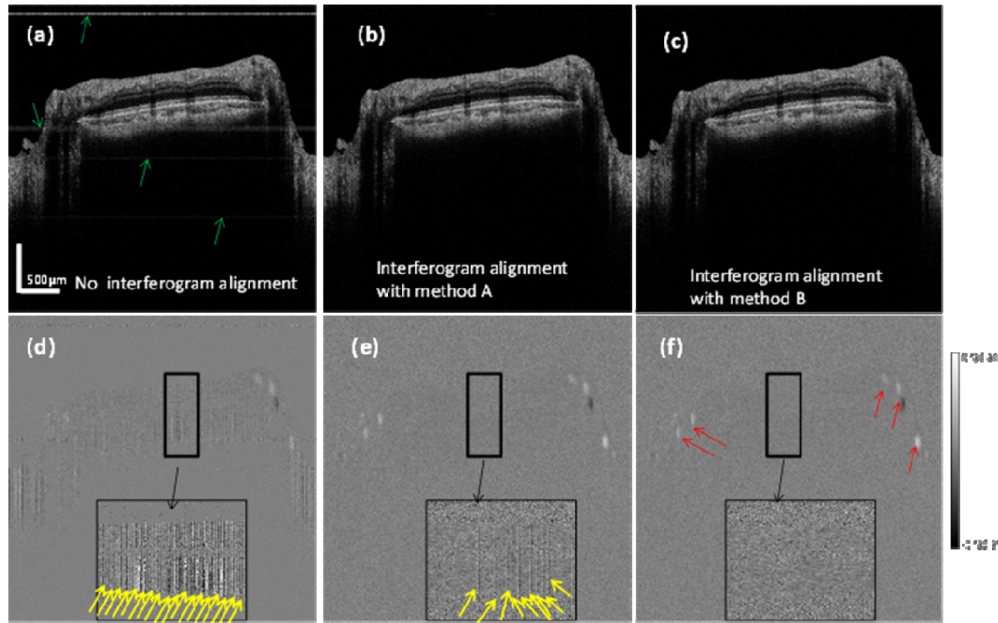


Fig. 4. OCT intensity (top row) and Doppler (bottom row) images of a normal human retina. The images contained 3200 interferograms acquired by a circular scan pattern with diameter of 1.5 mm around the optic disk region in a healthy volunteer. Typical FD-OCT processing steps without interferogram alignment were used to obtain the figure (a). Firstly, the DC and lower frequency offset for each interferogram is removed by subtracting the mean of background interferograms. Then Gaussian-window spectral shaping, numerical dispersion compensation and inverse fast Fourier transform were applied. In (a), the green arrows indicate the residual fixed-pattern noise. To get figure (b), all the interferograms were re-aligned with the phase-based method A and FD-OCT processing steps were applied after that. In Figure (c), all the interferograms were re-aligned with the intensity-based method B and typical FD-OCT processing steps were applied after that. Figures (d), (e) and (f) are the corresponding Doppler OCT images for (a), (b) and (c). In Figs. (d), (e) and (f), the region indicated by the small black rectangle was utilized for the performance evaluation. The insets indicated by the large black rectangle are the magnified images of the smaller rectangle and used for the phase stability evaluation. The yellow arrows indicate the locations that have residual phase errors induced by trigger jitter. More reduced residual phase errors are found in (e) as compared to (d). No residual phase error is found in (f). The red arrows in (f) show blood vessels.

The effect of fixed-pattern noise removal and phase stability improvement can be seen from the human retinal OCT intensity and Doppler images shown in Fig. 4. The images are from 3200 interferograms acquired by a circular scan pattern with diameter of 1.5 mm around the optic disk region. Figure 4(a) shows results from typical FD-OCT processing procedures without wavenumber alignment. After wavenumber alignment, the residual fixed-pattern noise artifacts, as indicated by green arrows in Fig. 4(a), were greatly reduced as shown in Figs. 4(b) and 4(c). Laser trigger jitter induced phase instability, which manifests as depth dependent phase difference as shown in Fig. 4 (d), was greatly reduced as shown in Figs. 4(e) and 4(f). From the insets of Figs. 4(e) and 4(f), we observed that method B gave better results than method A. In Fig. 4(f), no residual phase error is found. However, method A required less processing time. For the alignment of 3200 interferograms, method A takes 0.2496 seconds and method B takes 20.4672 seconds using Matlab 2012a running on a laptop with an Intel Core i5-3340 CPU.

4. Doppler OCT imaging of a diabetic patient

The wavenumber alignment algorithm (intensity-based method B) was applied to the imaging of a diabetic patient with Doppler OCT. Baumann et al. proposed a numerical method to correct the trigger jitter induced phase instability [7]. In their method, the slope of the phase ramp was estimated based on the phase sampled at two different depths, and this slope was used to correct the trigger jitter induced phase instability. Because there are not two fixed strong signals far from zero delay in the system used in the study, the phases from the tissue signal pixels along the A-line were used to estimate the slope in this study. This modified fitting method is realized by a linear fitting of phase values along the A-line with exclusion of possible vessel pixels. It should be noted that the original method proposed by Bauman et al. should give better results.

We compared the signal-to-noise ratio (SNR) of the images between results from the modified fitting method and those from the wavenumber alignment algorithm proposed in this paper (Fig. 5). The two methods were used to process the same raw data, and the procedures to calculate the Doppler flow were the same except for the trigger jitter/bulk motion correction step. The SNR was defined as the ratio of average value in the signal region to the standard deviation of the signal in background area. For the OCT intensity image, the signal region is defined as the retinal tissue region. For the Doppler OCT image, the signal region is the retinal vessel, and the background is the static retinal tissue where the Doppler shift should be zero. Regions selections are same for the two methods (Fig. 5a). As shown in Fig. 5, the results from the proposed alignment algorithm show higher SNR for both the OCT intensity (43.45 vs 27.86, no unit) and Doppler OCT images (7.47 vs 6.65, no unit). The SNR of the OCT intensity image was improved because of less noise in the background (29.56 vs 74.48, no unit). The SNR of Doppler phase shift was improved because of the higher value of Doppler phase shift in vessel area (average = 1.51 vs 1.34, unit: rad). However, the standard deviation of Doppler phase shift in the static tissue is not different (0.20 Vs 0.20, unit: rad). This improved image quality will enhance the development of automated detection of retinal tissue/vessels and the accuracy of total retinal blood flow measurements. A future study will be conducted to investigate this.

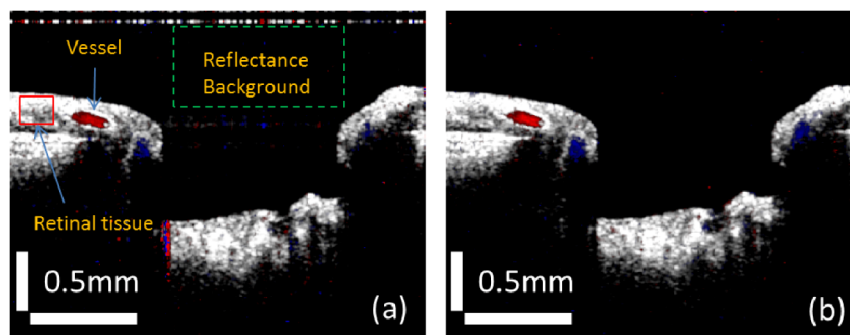


Fig. 5. Doppler OCT retinal image from a diabetic patient. The volume scan covered a $1.6 \times 2 \text{ mm}^2$ area of the optic disc and had 80 B-scans with 600 A-lines per B-scan. One cross section corresponding to a vertical line scan was selected to compare results between methods. (a) Cross section image obtained using Bauman's algorithm. Three regions were selected for signal-to-noise ratio (SNR) calculations. The SNR of Doppler phase shift (SNR_D) is the ratio of the average phase shift in a vessel and the standard deviation of the phase shift in static retinal tissue. The SNR of intensity (SNR_I) is the ratio of the average intensity in retina tissue and standard deviation of intensity in background. In this image, SNR_D = 6.65 and SNR_I = 27.86. (b) Cross section image obtained using wavenumber alignment method proposed here. In this image, SNR_D = 7.47 and SNR_I = 43.45.

5. Discussion

The proposed methods used the information at the residual fixed-pattern noise location to align the acquired interferograms so that residual fixed-pattern noise artifacts were removed and phase stability of the system was increased. Generally, these methods will work within the imaging range for all SS-OCT systems with residual fixed-pattern noise. To achieve the best performance, the location of the reference residual fixed-pattern noise should be around the zero frequency or close to the maximum imaging range of the system. Therefore, the sample image will not be overlapped with the reference residual fixed-pattern noise. However, if the system does not have residual fixed-pattern noise and one still desires to improve the system phase stability, an artificial fixed-pattern noise artifact may be generated. This could be achieved by adding a thin glass plate in the reference arm or using a calibration mirror with an OCT signal that appears in the imaging range of the system [3, 5–7].

Method B uses intensity/amplitude values as the cost function to find the relative wavenumber shift between two A-lines. It is more robust than the method A and could be used to reduce trigger jitter and improve the system phase stabilities in various situations. To demonstrate that, an OCT system (Fig. 6) with double delay lines in the reference arm was built. The two delay lines formed a Mach–Zehnder interferometer. One arm of the Mach–Zehnder interferometer was used to generate the fixed-pattern line in the image. The depth location of the fixed-pattern line can be tuned by changing the length of corresponding delay line. The same Axsun 1050 laser used in previous sections was used as light source. The signal from a balanced detector was sampled with a high speed digitizer (Alazar Technologies Inc., ATS 9350) using the built-in trigger and clock signals from the Axsun laser. Figure 7 shows the results of trigger jitter reduction with method B. An infrared viewing card was used as the sample. All of the images contain 256 A-lines. In the Fig. 7, a few situations are demonstrated. The fixed-pattern line is located close to the maximum imaging range of the system (row I), overlapped with sample image (row II), a result of 1st order coherence revival (row III), and a result of 2nd order coherence revival (row IV). The method B proposed here is able to successfully reduce the reduce trigger jitter and improve the system phase stabilities as demonstrated in columns c and d in Fig. 7. For the situation in row V of Fig. 7, there is no fixed-pattern noise (or line) in the images and the proposed method B is still able to reduce trigger jitter and improve the phase stability of the system. This is achieved by finding the relative wavenumber shift through minimizing the residual amplitudes of the sum of the first 20 pixels close to the zero delay. However, a few no residual phase errors are found as indicated by the blue arrows in Fig. 7 (row V column d).

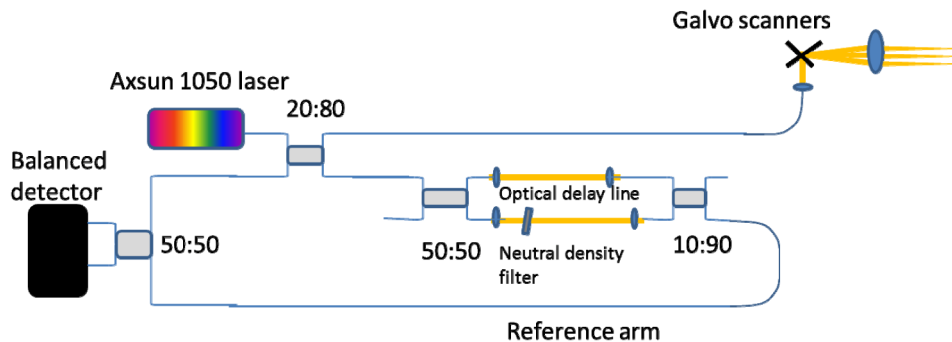


Fig. 6. Schematic of the OCT system with double delay lines in the reference arm. A Mach–Zehnder interferometer was used in the reference arm. One arm of the Mach–Zehnder interferometer was used to generate the fixed-pattern line in the image. The depth location of the fixed-pattern line can be tuned by changing the length of the corresponding delay line.

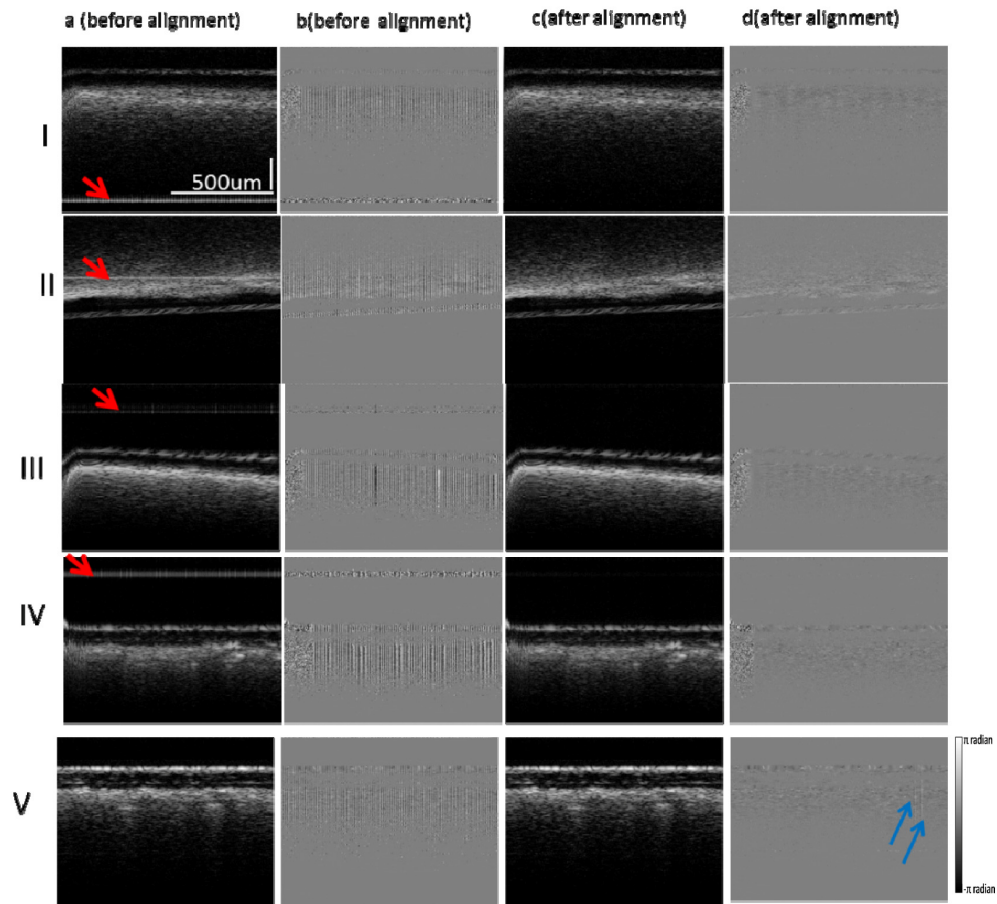


Fig. 7. Minimization of fixed-pattern artifact and reduction of trigger jitter using method B for various situations. Columns a and b show the structure and Doppler OCT images of a sample (an infrared sensor card) without interferogram alignment. Columns c and d show the structure and Doppler OCT images of the sample after interferogram alignment using method B. The red arrows show the location of fixed-pattern lines. In row I, the fixed-pattern line is close to the maximum imaging range of the system. In row II, the fixed-pattern line is overlaid with sample image. In row III, the fixed-pattern line is a result of 1st order coherence revival. In row IV, the fixed-pattern line is a result of 2nd order coherence revival. In row V, there is no fixed-pattern noise and the residual amplitude for the sum of the first 20 pixels close to the zero delay was minimized with method B to reduce trigger jitter and improve the phase stability of the system.

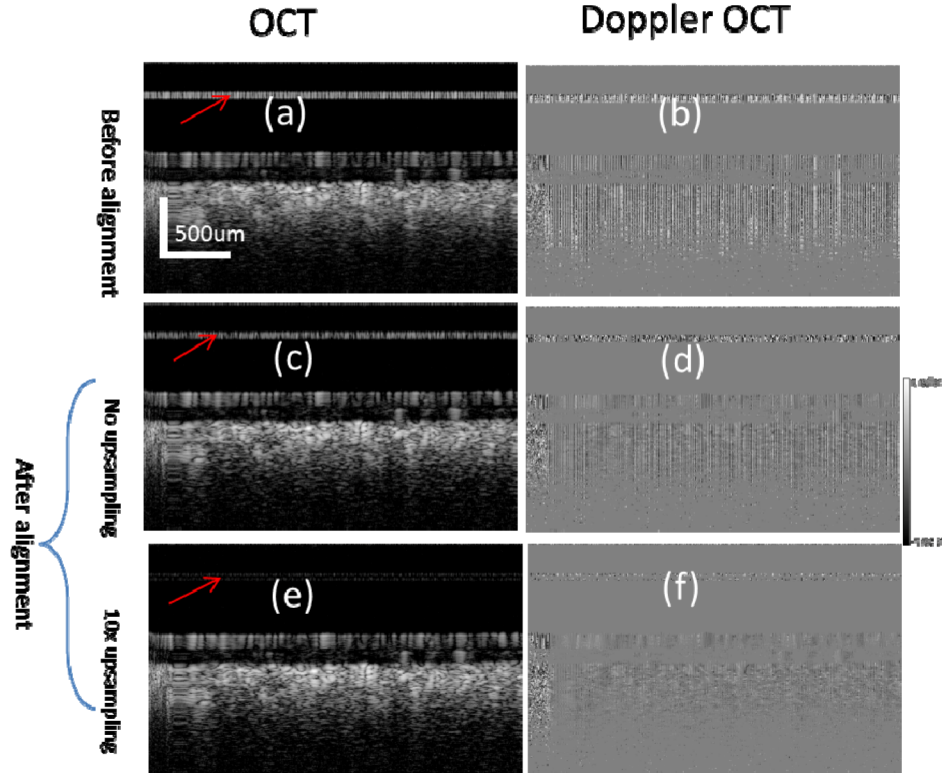


Fig. 8. Minimization of fixed-pattern artifact and reduction of trigger jitter using method B for a system with a constant sampling clock instead of an external optical k-clock. The OCT (a, b and e) and Doppler OCT (b, d and f) images of an infrared viewing card obtained before (a and b) and after (c,d,e and f) interferogram alignment are shown. Figures (c) and (d) are the OCT and Doppler OCT images after interferogram alignment on the original interferograms. Figures (e) and (f) are the OCT and Doppler OCT images after interferogram alignment on the 10 times upsampled interferograms. The images are obtained by direct Fourier transformation of the interferograms without resampling to a linear k-space. The reds arrows show location the fixed-pattern noise.

For SS-OCT systems that acquire the A-line interferograms with a constant sampling clock (either from the digitizer or from external constant clock) instead of an external optical k-clock, the relative shift between two interferograms may not be an integer multiple of the sampling interval. The proposed methods can also reduce trigger jitter and improve the phase stability of such a system. However, the methods proposed here are not able to fully solve the phase instability issue for this situation. Figure 8 shows the results. The system shown in Fig. 6 was used here and the A-line interferograms were acquired with the constant sampling clock(125MS/s) from the digitizer and the built-in A-line trigger from the laser. There were 1120 data points in an A_line interferogram. A static infrared view card was used as the sample. Method B was used here to align the A-line interferograms. It can be seen that the fixed-pattern line in Fig. 8(c) is much weaker than that in Fig. 8(a) and phase noise in Fig. 8(d) is weaker than that in Fig. 8(b). These results demonstrate that the method can be used to improve the image quality of SS-OCT systems without using an optical k-clock. However, to fully stabilize the system phase with the current method, upsampling of the original A-line interferograms is needed to get sub-point shift accuracy. Figures 8(c) and 8(d) show the results after applying the method B to 10 times upsampled A-line interferograms. A interpolation method based on frequency shifting and zero padding is used to upsample the interferograms [10]. Great improvement on the results can be found in Figs. 8(e) and 8(f).

The scaling factor $\xi(m_s, z)$ is the periodic function of $m_s \cdot z_f$. If N/z_f is an integer, there are a number of m_s that will make the scaling factor equal to zero. For example, if $N/z_f = 5$, any $m_s = 5 \cdot n$ will make scaling factor zero. This may limit the maximum number of k-shift that the method B can find. In an OCT system, the point spread function will usually take a few pixels instead of a single pixel and the fixed-pattern noise will usually take a few depth pixels in the image. So the correct relative k-shift can still be found by evaluating the sum of the A-line amplitude over a few pixels centered at z_f .

6. Conclusions

In conclusion, methods of aligning interferograms in order to reduce the fixed-pattern noise and improve phase stability of a SS-OCT system were proposed. Based on the information (amplitude/phase) of a scaling factor at the fixed-pattern noise location, the relative wavenumber shifts between the interferograms of interest and a reference interferogram were found and then used to align the interferograms to the reference interferogram. A system utilizing the wavenumber alignment algorithm was demonstrated for human retinal OCT and Doppler OCT imaging. These methods are purely numerical corrections for systems with fixed-pattern noise. They can be easily realized for SS-OCT systems without fixed-pattern noise.

Acknowledgments

This work was supported by Oregon Health & Science Foundation, NIH R01EY023285, NIH T32EY23211 and an unrestricted grant from Research to Prevent Blindness (New York, NY).